Title

A single-projection three-dimensional reconstruction algorithm for scanning transmission electron microscopy data

Authors

Brown, Hamish G
Pelz, Philipp M
Hsu, Shang-Lin
et al.

Publication Date

2020-11-15

Peer reviewed

A three-dimensional reconstruction algorithm for scanning transmission electron microscopy data from thick samples

Hamish G. Brown,[1,*] Philipp M. Pelz,[1,2] Shang-Lin Hsu,[1,2] Zimeng Zhang,[2] Ramamoorthy Ramesh,[2,3] Katherine Inzani,[4,5] Evan Sheridan,[4,5,6] Sinéad M. Griffin,[4,5] Scott D. Findlay,[7] Leslie J. Allen,[8] Mary C. Scott,[1,2] Colin Ophus,[1,†] and Jim Ciston[1,‡]

[1] *National Center for Electron Microscopy Facility, Molecular Foundry, Lawrence Berkeley National Laboratory, Berkeley, California 94720, USA*
[2] *Department of Materials Science and Engineering, University of California, Berkeley, CA, 94720, USA*
[3] *Department of Physics, University of California, Berkeley, California 94720, USA.*
[4] *Materials Sciences Division, Lawrence Berkeley National Laboratory, Berkeley, California 94720, USA*
[5] *Molecular Foundry, Lawrence Berkeley National Laboratory, Berkeley, California 94720, USA*
[6] *Theory and Simulation of Condensed Matter, Department of Physics, King's College London, The Strand, London WC2R 2LS, UK.*
[7] *School of Physics and Astronomy, Monash University, Victoria 3800, Australia*
[8] *School of Physics, University of Melbourne, Parkville, Victoria 3010, Australia*

(Dated: November 17, 2020)

Increasing interest in three-dimensional nanostructures adds impetus to electron microscopy techniques capable of imaging at or below the nanoscale in three dimensions. We present a reconstruction algorithm that takes as input a focal series of four-dimensional scanning transmission electron microscopy (4D-STEM) data and transcends the prevalent structure retrieval algorithm assumption of a very thin specimen homogenous along the optic axis. We demonstrate this approach by reconstructing the different layers of a lead iridate ($Pb_2Ir_2O_7$) and yttrium-stabilized zirconia ($Y_{0.095}Zr_{0.905}O_2$) heterostructure from data acquired with the specimen in a single plan-view orientation, with the epitaxial layers stacked along the beam direction.

There has recently been significant interest in nanoscale three-dimensional materials such as polarization vortices in layered $PbTiO_3$-$SrTiO_3$ heterostructures [1], van der Waals heterostructures [2] and strain-engineered nanoparticles [3]. Development of these materials is assisted by imaging techniques capable of three-dimensional characterisation at nanometer resolution. However, a limitation of three dimensional imaging techniques such as electron tomography [4] and current optical sectioning methods in scanning transmission electron microscopy (STEM) [5, 6] is that they typically rely on annular dark-field (ADF) STEM which is often only sensitive to the heavy atoms within the sample. Techniques which reconstruct the electric potential of a sample from diffraction plane measurements of the modification of the electron probe after transmission through the specimen, such as differential phase contrast (DPC) STEM [7] and STEM ptychography [8–10], are alternatives that are sensitive to both light and heavy atoms. The take-up of these techniques has been accelerated by recent advances in segmented detectors [11] and the 4D-STEM technique – where full two dimensional diffraction patterns are recorded for a two dimensional raster scan of a STEM probe. The latter has been enabled by advanced electron cameras capable of reading out full diffraction patterns at frequencies of the order of 100s of Hertz or greater, approaching the typical dwell times of a focused STEM probe [12]. In their most common implementations, ptychography and DPC assume that interaction occurs in a single spatial plane – referred to as the projection or phase object approximation – and thus these methods are generally inappropriate for strongly scattering materials thicker than a few nanometers.

This Letter discusses a three-dimensional imaging technique capable of visualizing both light and heavy atoms in a thick sample with nanoscale depth selectivity. We reconstruct the scattering matrix ($\mathcal{S}$-matrix) – a mathematical formalism common in quantum scattering theory [13] that is capable of describing multiple electron scattering in an electron microscopy sample [14] – from a focal series of 4D-STEM measurements and then use this $\mathcal{S}$-matrix to synthesize images of the specimen at different focal planes. Using this technique, we demonstrate the visibility of separate lead iridate, $Pb_2Ir_2O_7$ (PIO), and yttrium-stabilized zirconia, $Y_{0.095}Zr_{0.905}O_2$ (YSZ), layers in a PIO-YSZ heterostructure. This builds on previous work [15–19] on $\mathcal{S}$-matrix retrieval that focused on single crystal structures.

For a brief derivation of the $\mathcal{S}$-matrix formalism we take as our starting point the Schrödinger equation in reciprocal space for the electron wave function with a relativistic velocity along the z-direction, for which the paraxial approximation is appropriate. On a discretized grid with periodic boundary conditions [20], this equation is given by [21]

$$\frac{\partial \psi_{\mathbf{g}}}{\partial z} = -i\pi\lambda g^2 \psi_{\mathbf{g}}(z) + \sum_{\mathbf{h}} i\sigma V_{\mathbf{g}-\mathbf{h}}(z)\psi_{\mathbf{h}}(z)\,. \quad (1)$$

Here the Fourier coefficients of the electron wave function are given by $\psi_{\mathbf{g}}$ for reciprocal space coordinate $\mathbf{g}$ with amplitude g, λ is the electron wavelength, σ is the interaction constant in 1/Vm [22] and $V_{\mathbf{g-h}}(z)$ are the 2D Fourier coefficients of the electrostatic potential at each depth z in the sample. From Eq. (1) we can construct a matrix first-order differential equation,

$$\frac{\partial \boldsymbol{\psi}(z)}{\partial z} = i\mathcal{A}(z)\boldsymbol{\psi}(z), \tag{2}$$

where $\boldsymbol{\psi}$ is a column vector containing the Fourier coefficients of the electron wave function. We write the entries of the matrix $\mathcal{A}$, the structure matrix, for an entry corresponding to the Fourier coefficients $\mathbf{g}$ of the scattered electron wave and $\mathbf{h}$ of the incoming electron wave as,

$$\mathcal{A}_{\mathbf{g},\mathbf{h}}(z) = -\pi\lambda g^2\delta_{\mathbf{g-h}} + \sigma V_{\mathbf{g-h}}(z). \tag{3}$$

In the absence of any scattering potential (i.e. $V_{\mathbf{g-h}}(z) = 0$) the diagonal terms, $-\pi\lambda g^2\delta_{\mathbf{g-h}}$ where $\delta_{\mathbf{g-h}}$ is the Kronecker delta, have an equivalent effect to the Fresnel free-space propagator. A standard solution to Eq. (3) is the $\mathcal{S}$-matrix solution,

$$\boldsymbol{\psi}(z+\Delta z) = e^{i\Delta z\mathcal{A}(z)}\boldsymbol{\psi}(z) = \mathcal{S}(\Delta z)\boldsymbol{\psi}(z)\,. \tag{4}$$

It is implicitly assumed in Eq. (4) that $V_{\mathbf{g-h}}(z)$ is constant over thickness Δz. Where $V_{\mathbf{g-h}}(z)$ varies with thickness, the $\mathcal{S}$-matrix can be constructed as a product of $\mathcal{S}$-matrices over n thinner sub-regions within which the z variation of $V_{\mathbf{g-h}}(z)$ is minimal,

$$\mathcal{S}(z) = \prod_{i=0}^{n-1}\mathcal{S}(z_{i+1}-z_i). \tag{5}$$

In a 4D-STEM experiment the diffraction pattern for each raster scan position of a focused probe is measured and, for a probe position $\mathbf{R}$ and diffraction coordinate $\mathbf{g}$, this diffraction pattern can be calculated using the $\mathcal{S}$-matrix as

$$I(\mathbf{g},\mathbf{R},\Delta f) = \left|\sum_{\mathbf{h}}\mathcal{S}_{\mathbf{g},\mathbf{h}}A(\mathbf{h})e^{-2\pi i\mathbf{h}\cdot\mathbf{R}-i\pi h^2\Delta f}\right|^2. \tag{6}$$

Here Δf is the probe defocus relative to the entrance surface of the specimen and $A(\mathbf{h})$ is the aperture function, a top-hat function that is 1 for Fourier components within the aperture, $|\mathbf{h}| < h_{\max} = \alpha/\lambda$ (α is the probe convergence semi-angle in radians), and 0 otherwise. We seek to recover the (complex-valued) $\mathcal{S}$-matrix for a set of (real-valued) 4D-STEM datasets $I(\mathbf{g},\mathbf{R},\Delta f)$ recorded for a number of scan positions $\mathbf{R}$ and defoci Δf, a phase retrieval problem which we solve using a gradient descent approach [23–26], see Fig. S1 in the supplementary materials (SM).

The specimen potential $V(x,y,z)$ would ideally be directly retrieved from the $\mathcal{S}$-matrix resulting from the phase-retrieval step, and previous work has identified a quantitative method of doing this for a perfect crystalline sample [15, 16, 19] and demonstrated the technique experimentally [18]. Here we consider the general case of a more heterogeneous sample such as a heterostructure or nanoparticle where there is currently no direct method for solving this problem. We therefore use an optical sectioning approach that estimates the potential at a given depth of the object [27].

Consider $\mathcal{S}_{\mathbf{r},\mathbf{h}}$ (the $\mathcal{S}$-matrix component that maps plane wave input $\mathbf{h}$ to a real-space exit surface wave function [28]) for the case indicated in Fig. 1(a), freespace propagation through distance z_0, phase object interaction with potential (e.g. an atom), and further propagation through distance $\Delta z = z_1 - z_0$,

$$\mathcal{S}_{\mathbf{r},\mathbf{h}} = \mathcal{P}(\mathbf{r},\Delta z)\otimes_{\mathbf{r}}\left[e^{i\sigma V(\mathbf{r})}e^{-i\pi\lambda h^2 z_0}e^{2\pi i\mathbf{h}\cdot\mathbf{r}}\right]. \tag{7}$$

Here $\mathcal{P}(\mathbf{r},\Delta z)$ is the real space representation of the Fresnel free-space propagator for propagation of distance Δz. Using the convolution theorem, Eq. (7) can be written as the inverse Fourier transform of the product of the Fourier transforms of the individual expressions:

$$\mathcal{S}_{\mathbf{r},\mathbf{h}} = e^{-i\pi\lambda z_0 h^2}\int e^{-i\pi\lambda\Delta z h^2}\hat{T}_{\mathbf{g-h}}e^{2\pi i\mathbf{g}\cdot\mathbf{r}}d\mathbf{g} \tag{8}$$

where we have defined $\hat{T}_{\mathbf{g}} = \mathcal{F}_{\mathbf{r}\to\mathbf{g}}\left[e^{i\sigma V(\mathbf{r})}\right]$ and made use of the Fourier shift theorem. Making the change of variable $\mathbf{g}\to\mathbf{g}+\mathbf{h}$, Eq. (8) becomes

$$\begin{aligned}\mathcal{S}_{\mathbf{r},\mathbf{h}} &= e^{-i\pi\lambda z_0 h^2}\int e^{-i\pi\lambda\Delta z(\mathbf{g}+\mathbf{h})^2}\hat{T}_{\mathbf{g}}e^{2\pi i(\mathbf{g}+\mathbf{h})\cdot\mathbf{r}}d\mathbf{g} &(9)\\ &= e^{2\pi i\mathbf{h}\cdot\mathbf{r}}e^{-i\pi\lambda z_1 h^2}\\ &\quad\times\int e^{-i\pi\lambda\Delta z g^2}\hat{T}_{\mathbf{g}}e^{-2\pi i\mathbf{g}\cdot(\lambda\Delta z\mathbf{h})}e^{2\pi i\mathbf{g}\cdot\mathbf{r}}d\mathbf{g} &(10)\end{aligned}$$

Invoking the convolution theorem and Fourier shift theorem again (in reverse form to that used previously), this becomes,

$$\mathcal{S}_{\mathbf{r},\mathbf{h}} = e^{2\pi i\mathbf{h}\cdot\mathbf{r}-i\pi\lambda z_1 h^2}\left[\mathcal{P}(\mathbf{r},\Delta z)\otimes_{\mathbf{r}}e^{i\sigma V(\mathbf{r}-\mathbf{h}\lambda\Delta z)}\right]. \tag{11}$$

For this case, the $\mathcal{S}$-matrix consists of the atom, shifted laterally a distance $\mathbf{h}\lambda\Delta z$ and propagated a distance Δz in free space [schematically shown in Fig. 1(a)] with a multiplicative phase ramp $e^{2\pi\mathbf{r}\cdot\mathbf{h}}$. To generate our optical section reconstruction at depth z, we apply the inverse of each of these processes (i.e. the phase ramp, propagation and paraxial shift) for each $\mathbf{h}$ in $\mathcal{S}_{\mathbf{r},\mathbf{h}}$, sum $\mathcal{S}_{\mathbf{r},\mathbf{h}}$ over all $\mathbf{h}$ and the phase of the result should be a reasonable approximation to $V(\mathbf{r})$. Averaging over the different momentum components $\mathbf{h}$ of the STEM probe provides some robustness against the effects of multiple scattering, although it is not addressed explicitly in the

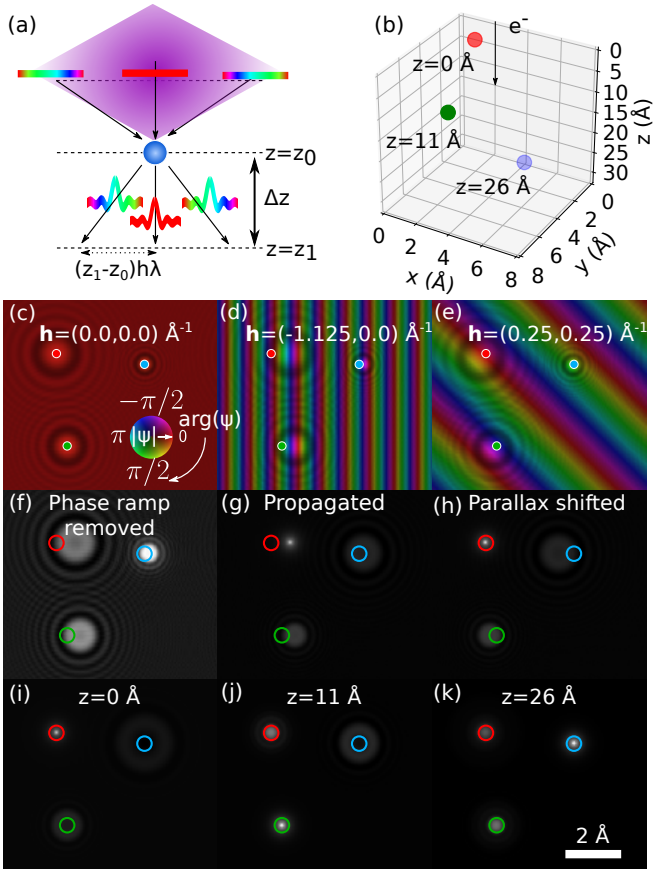

FIG. 1. Reconstructing three dimensional information from the $\mathcal{S}$-matrix. (a) For an atom at depth z_0, each component of the $\mathcal{S}$-matrix will acquire a phase through interaction with this atom. For the three oxygen atom model system shown in (b) the complex $\mathcal{S}$-matrix components for three different Fourier component inputs $\mathbf{h}$ are shown in (c-e) plotted with phase and intensity given by the color-wheel in (c). The reconstruction method described in the text involves (f) removing the phase ramp, (g) propagating the complex wave function back to the plane of interest and (h) correcting the parallax shift from propagation. Only the phase is plotted in gray-scale in these and following panels. Shown in (i)-(k) are the reconstructions for the respective planes of the different atoms.

depth sectioning part of the algorithm. This is analagous to the diminution of dynamical effects observed as a result of averaging diffraction patterns over different beam tilts in the precession electron diffraction technique [29].

We demonstrate this approach on a toy model consisting of three oxygen atoms which is shown in Fig. 1(b). Forward simulated $\mathcal{S}$-matrix components for different Fourier components $\mathbf{h}$ are shown in Figs. 1(c-e), plotted with phase and intensity given by the color-wheel in (c). The positions of the atoms projected onto the 2D plane are indicated with colored dots and the paraxial shift from these projected positions of each of these atoms is visible. Shown in the next row of Fig. 1, with now just the phase plotted in gray color scale, are first the removal of the phase ramp $e^{2\pi\mathbf{h}\cdot\mathbf{r}}$ in (f), the application of the propagation operator $\mathcal{P}(\mathbf{r}, -32\text{ Å})$ in (g) and finally, in (h), the correction of the paraxial shift $\lambda\Delta z\mathbf{h}$ to reconstruct the atom at nominal height $z = 0$ from Fig. 1(b). These steps are applied to all components of $\mathcal{S}_{\mathbf{r},\mathbf{h}}$ and summed over all $\mathbf{h}$, which as can be seen in Fig. 1(i) further diminishes the contributions of atoms at different depths to the plane of reconstruction. The process is repeated for the other two atoms in Figs. 1(j) and (k). The high spatial resolution exhibited in this reconstructions is the result of their reconstruction from a forward simulated $\mathcal{S}$-matrix – finite signal-to-noise and partial coherence of the STEM probe will limit the fidelity of reconstruction in the experimental case.

For an experimental demonstration, we used a PIO layer grown on a (001)-oriented YSZ substrate by pulsed laser deposition at a growth temperature of 600°C, wedge polished on the YSZ substrate side and then ion milled with a low-energy Ar^+ beam. Experiments were performed using the TEAM I instrument at the National Center for Electron Microscopy (NCEM) Facility of the Molecular Foundry, a double aberration-corrected Thermo-Fisher Titan 80-300. A 300 kV accelerating voltage and a 20 mrad probe forming aperture was used in experiment. To maximise source coherence and minimize beam damage, source magnification (the "spot size" software setting) was set to 10, the penultimate setting. A focal series of 4D-STEM data was recorded on a Gatan K3 direct-electron detector, operated in counting mode, at the end of a Gatan Continuum imaging filter with an energy slit width of 15 eV centered around the zero-loss peak. A probe step of 0.21 Å with probe dwell time of 0.874 ms and beam current of 2.01 pA (estimated by the K3 camera) was used. The reconstructed $\mathcal{S}$-matrix is sensitive to residual probe aberrations [18] so careful initial alignment of the probe corrector and tuning of stigmators immediately before 4D-STEM focal series acquisition was necessary. ADF STEM images, from a detector inner angle of 110 mrad, recorded concurrently with the 4D-STEM data are shown in Fig. 2(a). Alignment of the frames in the focal series was achieved by fitting the peaks of the atomic columns in the STEM ADF images [30] and smoothly deforming the probe positions to match a rectangular crystalline lattice rotated to the same average orientation as the fitted lattice as detailed in Fig. S2 of the SM. The region that was inputted into the $\mathcal{S}$-matrix reconstruction is shown with a dashed white outline in the ADF STEM results in Fig. 2(a). Defocus reported by the microscope software had to be adjusted by a multiplicative factor of 1.24, a value determined by comparing the geometric blur with defocus of gold nanoparticles embedded in amorphous carbon with the geometric blur expected from a 20 mrad probe forming aperture (see Fig. S3 of the SM).

The experimental $\mathcal{S}$-matrix was reconstructed using 10 iterations of the gradient descent algorithm described in

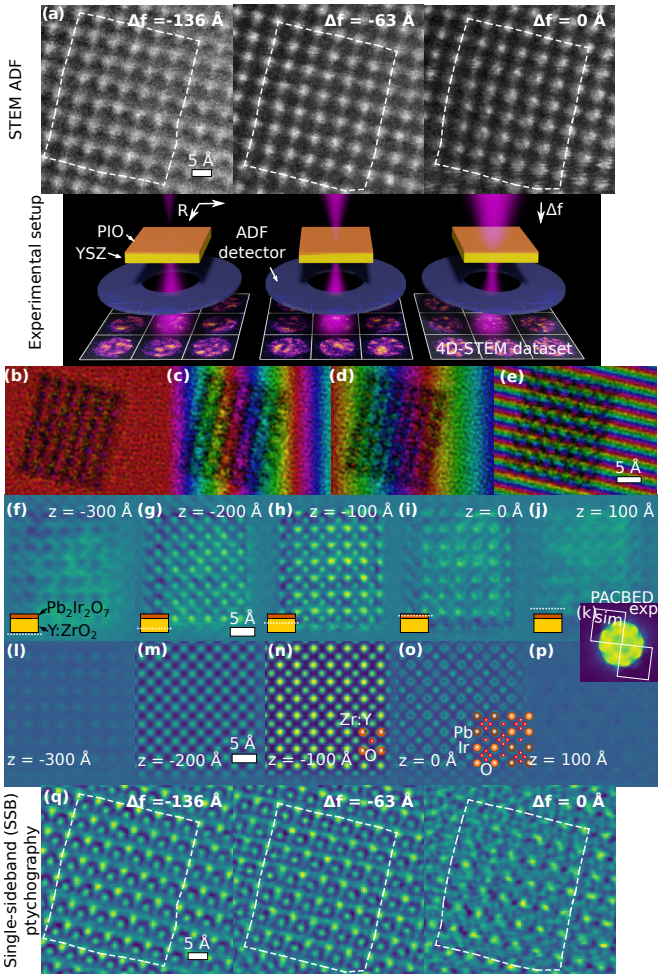

FIG. 2. Experimental reconstruction of the $\mathcal{S}$-matrix from a focal series of 4D-STEM scans of a PIO-YSZ heterostructure. Simultaneously acquired ADF STEM images are shown in (a). A select few components of the $\mathcal{S}$-matrix reconstructed from the 4D-STEM datasets are shown in (b)-(e). The optical section reconstructed from this $\mathcal{S}$-matrix is shown in (f)-(j) with the 150 Å YSZ substrate visible in (g) and (h) and the 50 Å thick PIO layer visible in panel (i). Panels (f) and (j) are from focal planes outside of the sample. Experimental and simulated position-averaged convergent beam electron diffraction (PACBED) pattern in (k) provides additional supporting evidence that the structure is indeed a structure of thickness indicated by the depth section. Panels (l)-(p) are from a reconstruction from simulated data of such a structure. Single-sideband (SSB) ptychography reconstructions from the 4D-STEM dataset are shown in (q).

Fig. S1 of the SM. Convergence with increasing iterations of the algorithm is shown in Fig. S4 of the SM. Select components of the $\mathcal{S}$-matrix are shown in Figs. 2(b)-(e), and optical sectioning applied to the results. Optical sections at 100 Å intervals are shown in Figs. 2(f)-(j). The −300 Å and 100 Å sections are outside the bounds of the object, though the lattice is still faintly visible. The presence of Pb and Ir in the upper layers of the heterostructure is evidenced by appearance of "caldera" or volcano like atomic contrast in Fig. 2(i). It is commonly seen in phase reconstructions in STEM that the phase imparted on an electron wave by high Z atomic columns, which strongly elastically and inelastically scatter the electron probe, are observed to underestimate the true scattering potential of an object leading to a dip in the reconstructed phase close to the atomic position [31]. Thus the Pb and Ir atoms ($Z = 82$ and $Z = 77$) are observed to be darker in the reconstruction than the lighter Y and Zr atoms ($Z = 39$ and $Z = 40$). From the optical section we estimate the thickness to be 200 Å with a composition of approximately 50 Å of PIO and 150 Å of YSZ. This is supported by comparison of the scan position-averaged convergent beam electron diffraction (PACBED) pattern [32] from experiment with that simulated for an equivalent model structure of PIO-YSZin (k).

Figs. 2(l)-(p) show the results of simulating and then reconstructing a model structure with 50 Å of PIO and 150 Å of YSZ for equivalent focal conditions to the experimental data in Figs. 2(f)-(j), showing good overall qualitative agreement with experiment. An experimental reconstruction from a much thinner region of the sample, free of PIO, is shown in Fig. S5 of the SM and caldera-like atoms are not visible in that reconstruction.

Phase reconstructions from single sideband (SSB) ptychography STEM, calculated from the 4D-STEM dataset, are shown in (q). As was the case with the $\mathcal{S}$-matrix reconstruction, SSB reveals the oxygen columns in the PIO-YSZ structure which are invisible in the ADF STEM images of Fig. 2(a) and suggests, in the $\Delta f = 0$ Å image, that the dataset was recorded in a region of the specimen where the PIO layer terminates, with the upper left region of the image apparently only containing the YSZ substrate. This is consistent with the optical section in Fig. 2(i) showing stronger evidence of Pb and Ir atoms in the bottom right than in the upper left of the reconstruction. A differential phase contrast (DPC) STEM reconstruction of the datacube produces similar results to SSB ptychography, see Fig. S6 of the SM.

A final point to note is that PIO is a pyrochlore structure and, when projected down its [001] crystallographic zone-axis, the oxygen columns should exhibit alternating centered and delocalized columns, as shown in the structural overlay of Fig. 2(o). This was not visible in this reconstruction of the $Pb_2Ir_2O_7$ structure, nor in any of the annular bright-field (ABF) STEM images synthesized from the 4D-STEM datasets, seen in Fig. S7(a) of the SM.

To account for this, density functional theory (DFT) calculations were performed to determine the extent of compositional and structural influences on the oxygen positions. We use the parameter x to describe the position of O on the Wyckoff site $48f$ $(x,\frac{1}{8},\frac{1}{8})$ of the $Fd\bar{3}m$ (No. 227-2) space group, where x=0.375 gives a centered

oxygen column and x=0.3125 is the maximum amount of oxygen off-centering allowed in the pyrochlore structure [33]. Values of x for different structural variations are given in Table I. Incorporating biaxial strain, stoichiometry variations (through the inclusion of oxygen vacancies) and an explicit YSZ/PIO interface do not cause in significant changes in x. For 37.5% cation antisite defects, there is a considerable increase in x, indicating that a large proportion of antisite defects could induce a noticable change to the alternating pattern. Simulated STEM images of this amount of disorder are shown in Fig. S7 with high levels of disorder (50% cation antisites) providing reasonable agreement with ABF-STEM experiment. ABF-STEM images from a sample of the same material prepared such that the PIO-YSZ interface could be viewed in cross-section revealed regions where the alternating centered and delocalized oxygen columns were visible and areas where adjacent oxygen columns appeared centered (see SM Fig. S8). This suggests that alternating oxygen column order is likely present in layered nanodomains within the sample. Cation disorder, either from the growth process or damage to the specimen during ion milling, can modify local layered oxygen order and is not noticeable when the sample is viewed in plan-view projection in the electron microscope.

Structural variation	x
$Pb_2Ir_2O_7$	0.330
$Pb_2Ir_2O_7$ biaxially strained to 10.28 Å	0.332
PIO(001)/YSZ(001) interface	0.332
$Pb_2Ir_2O_{6.5}$	0.327-0.329
$Pb_2Ir_2O_6$	0.327
$Pb_2Ir_2O_7$ with % cation antisites,	average x
12.25%	0.336
25.0%	0.337
37.5%	0.344
50.0%	0.342

TABLE I. Oxygen position parameter x, describing oxygen column delocalization in the pyrochlore structure, calculated from DFT structural optimizations with strain, interface, and compositional variations.

This Letter has demonstrated a new electron microscopy technique capable of imaging light and heavy atoms in thicker, strongly scattering electron microscopy specimens using 4D-STEM data recorded in a single specimen orientation. This opens up new avenues for the study of three dimensional nanostructures with the ability to study structural changes in light and heavy atom positions through thickness.

Work at the Molecular Foundry was supported by the Office of Science, Office of Basic Energy Sciences, of the U.S. Department of Energy under Contract No. DE-AC02-05CH11231. J.C. and H.G.B. acknowledge support from the Presidential Early Career Award for Scientists and Engineers (PECASE) through the U.S. Department of Energy. P.M.P. was primarily supported by STROBE: A National Science Foundation Science & Technology Center under Grant No. DMR 1548924. S.M.G., E.S. and K.I. were supported by the Laboratory Directed Research and Development Program of LBNL under the U.S. Department of Energy Contract No. DE-AC02-05CH11231. E.S. acknowledges support from the US-Irish Fulbright Commission and work supported by the Air Force Office of Scientific Research under award number FA9550-18-1-0480. C.O. acknowledges support from the U.S. Department of Energy Early Career Research Program. Computational resources were provided by the National Energy Research Scientific Computing Center and the Molecular Foundry. This research was partly supported under the Discovery Projects funding scheme of the Australian Research Council (Project No. FT190100619).

All electron microscopy simulation and data-processing and reconstruction software used in this publication is available in the SM. Due to their large size, experimental datasets are not hosted along with the publication but can readily be made available upon request.

* Current address: Advanced Microscopy Facility, Bio21 Molecular Science and Biotechnology Institute, the University of Melbourne, Victoria 3052, Australia; hgbrown@unimelb.edu.au
† cophus@gmail.com
‡ jciston@lbl.gov

[1] A. Yadav, C. Nelson, S. Hsu, Z. Hong, J. Clarkson, C. Schlepütz, A. Damodaran, P. Shafer, E. Arenholz, L. Dedon, *et al.*, Observation of polar vortices in oxide superlattices, Nature **530**, 198 (2016).
[2] F. Withers, O. Del Pozo-Zamudio, A. Mishchenko, A. P. Rooney, A. Gholinia, K. Watanabe, T. Taniguchi, S. J. Haigh, A. Geim, A. I. Tartakovskii, *et al.*, Light-emitting diodes by band-structure engineering in van der waals heterostructures, Nature Materials **14**, 301 (2015).
[3] M. H. Oh, M. G. Cho, D. Y. Chung, I. Park, Y. P. Kwon, C. Ophus, D. Kim, M. G. Kim, B. Jeong, X. W. Gu, *et al.*, Design and synthesis of multigrain nanocrystals via geometric misfit strain, Nature **577**, 359 (2020).
[4] Y. Yang, C.-C. Chen, M. Scott, C. Ophus, R. Xu, A. Pryor, L. Wu, F. Sun, W. Theis, J. Zhou, *et al.*, Deciphering chemical order/disorder and material properties at the single-atom level, Nature **542**, 75 (2017).
[5] K. van Benthem, A. R. Lupini, M. P. Oxley, S. D. Findlay, L. J. Allen, and S. J. Pennycook, Three-dimensional ADF imaging of individual atoms by through-focal series scanning transmission electron microscopy, Ultramicroscopy **106**, 1062 (2006).
[6] H. L. Xin and D. A. Muller, Aberration-corrected ADF-STEM depth sectioning and prospects for reliable 3D imaging in S/TEM, Journal of Electron Microscopy **58**, 157 (2009).
[7] N. Shibata, T. Seki, G. Sánchez-Santolino, S. D. Findlay, Y. Kohno, T. Matsumoto, R. Ishikawa, and Y. Ikuhara,

Electric field imaging of single atoms, Nature Communications **8**, 1 (2017).
[8] P. D. Nellist, B. C. McCallum, and J. M. Rodenburg, Resolution beyond the "information limit" in transmission electron microscopy, Nature **374**, 630 (1995).
[9] H. Yang, R. Rutte, L. Jones, M. Simson, R. Sagawa, H. Ryll, M. Huth, T. Pennycook, M. Green, H. Soltau, *et al.*, Simultaneous atomic-resolution electron ptychography and Z-contrast imaging of light and heavy elements in complex nanostructures, Nature Communications **7**, 1 (2016).
[10] Y. Jiang, Z. Chen, Y. Han, P. Deb, H. Gao, S. Xie, P. Purohit, M. W. Tate, J. Park, S. M. Gruner, *et al.*, Electron ptychography of 2D materials to deep sub-ångström resolution, Nature **559**, 343 (2018).
[11] N. Shibata, Y. Kohno, S. D. Findlay, H. Sawada, Y. Kondo, and Y. Ikuhara, New area detector for atomic-resolution scanning transmission electron microscopy, Journal of Electron Microscopy **59**, 473 (2010).
[12] C. Ophus, Four-dimensional scanning transmission electron microscopy (4D-STEM): from scanning nanodiffraction to ptychography and beyond, Microscopy and Microanalysis **25**, 563 (2019).
[13] S. Weinberg, *The Quantum Theory of Fields*, Vol. 2 (Cambridge university press, 1995).
[14] L. Sturkey, The calculation of electron diffraction intensities, Proceedings of the Physical Society **80**, 321 (1962).
[15] J. Spence, Direct inversion of dynamical electron diffraction patterns to structure factors, Acta Crystallographica Section A: Foundations of Crystallography **54**, 7 (1998).
[16] L. J. Allen, H. M. L. Faulkner, and H. Leeb, Inversion of dynamical electron diffraction data including absorption, Acta Crystallographica Section A: Foundations of Crystallography **56**, 119 (2000).
[17] S. D. Findlay, Quantitative structure retrieval using scanning transmission electron microscopy, Acta Crystallographica Section A: Foundations of Crystallography **61**, 397 (2005).
[18] H. G. Brown, Z. Chen, M. Weyland, C. Ophus, J. Ciston, L. J. Allen, and S. D. Findlay, Structure retrieval at atomic resolution in the presence of multiple scattering of the electron probe, Physical Review Letters **121**, 266102 (2018).
[19] J. J. Donatelli and J. C. H. Spence, Inversion of many-beam Bragg intensities for phasing by iterated projections: Removal of multiple scattering artifacts from diffraction data, Physical Review Letters **125**, 065502 (2020).
[20] Which is exact for a crystal and a good approximation for a non-periodic object if the field of view is sufficiently large in real space and with fine enough sampling.
[21] W. Coene and D. Van Dyck, Inelastic scattering of high-energy electrons in real space, Ultramicroscopy **33**, 261 (1990).
[22] The interaction constant is given by $\sigma = 2\pi m_e e\lambda/h^2$ where m_e, e and h are the mass of an electron, the charge of an electron and Planck's constant respectively.
[23] M. Guizar-Sicairos and J. R. Fienup, Phase retrieval with transverse translation diversity: a nonlinear optimization approach, Optics Express **16**, 7264–7278 (2008).
[24] P. Thibault and M. Guizar-Sicairos, Maximum-likelihood refinement for coherent diffractive imaging, New J. Phys. **14**, 063004 (2012).
[25] G. Wang, G. B. Giannakis, and Y. C. Eldar, Solving systems of random quadratic equations via truncated amplitude flow, IEEE Transactions on Information Theory **64**, 773 (2017).
[26] P. M. Pelz, H. G. Brown, J. Ciston, S. D. Findlay, Y. Zhang, M. Scott, and C. Ophus, Reconstructing the scattering matrix from scanning electron diffraction measurements alone, arXiv preprint arXiv:2008.12768 (2020).
[27] C. Ophus, T. R. Harvey, F. S. Yasin, H. G. Brown, P. M. Pelz, B. H. Savitzky, J. Ciston, and B. J. McMorran, Advanced phase reconstruction methods enabled by four-dimensional scanning transmission electron microscopy, Microscopy and Microanalysis **25** (Suppl. 2), 10 (2019).
[28] The $\mathcal{S}$-matrix is a mathematical construct common in quantum physics that maps the input momentum states (i.e. Fourier components of the wavefunction) of the incoming particle to the output momentum states [13]. In this Letter we often use a real space representation of this quantity which is related to the more conventional representation of the $\mathcal{S}$-matrix via an inverse Fourier transform operation ($\mathcal{S}_{\mathbf{r},\mathbf{h}} = \mathcal{F}^{-1}_{\mathbf{g}\to\mathbf{r}}\mathcal{S}_{\mathbf{g},\mathbf{h}}$).
[29] J. Ciston, B. Deng, L. D. Marks, C. S. Own, and W. Sinkler, A quantitative analysis of the cone-angle dependence in precession electron diffraction, Ultramicroscopy **108**, 514 (2008).
[30] M. Nord, P. E. Vullum, I. MacLaren, T. Tybell, and R. Holmestad, Atomap: a new software tool for the automated analysis of atomic resolution images using two-dimensional Gaussian fitting, Advanced Structural and Chemical Imaging **3**, 9 (2017).
[31] R. Close, Z. Chen, N. Shibata, and S. Findlay, Towards quantitative, atomic-resolution reconstruction of the electrostatic potential via differential phase contrast using electrons, Ultramicroscopy **159**, 124 (2015).
[32] J. M. LeBeau, S. D. Findlay, L. J. Allen, and S. Stemmer, Position averaged convergent beam electron diffraction: Theory and applications, Ultramicroscopy **110**, 118 (2010).
[33] M. Subramanian, G. Aravamudan, and G. Subba Rao, Oxide pyrochlores — A review, Progress in Solid State Chemistry **15**, 55 (1983).